International Journal of Heat and Mass Transfer 52 (2009) 1012–1022

Contents lists available at ScienceDirect

International Journal of Heat and Mass Transfer

journal homepage: www.elsevier.com/locate/ijhmt

# Hybrid DNS/LES of high Schmidt number mass transfer across turbulent air–water interface

Yosuke Hasegawa *, Nobuhide Kasagi

*Department of Mechanical Engineering, The University of Tokyo, Hongo 7-3-1, Bunkyo-ku, Tokyo 113-8656, Japan*

ARTICLE INFO

*Article history:*
Received 19 March 2007
Received in revised form 28 May 2008
Available online 2 September 2008

*Keywords:*
Turbulence
Air–water interface
Mass transfer
Schmidt number
Surface divergence

ABSTRACT

Numerical simulation of a coupled air–water turbulent flow and associated high Schmidt number mass transfer is carried out via a hybrid scheme of direct and large-eddy simulations (DNS/LES). Due to the large density ratio of water and air, the dynamical coupling between the air and water turbulent flows is found to be weak at the low wind velocity considered here. Instead, the self-sustaining mechanisms due to the mean shear, which are similar to those near a solid wall, are dominant even close to the air–water interface. The spatio-temporal correlations between the local mass transfer rate and velocity fluctuations around the interface reveal that impingement of fresh water on the interface governs the interfacial mass transfer. It is found that the local mass transfer rate can be predicted from the surface divergence by the Chan and Scriven's stagnation flow model. This explains why the mass transfer rate is well correlated with the intensity of the surface divergence under a variety of flow conditions.



## 1. Introduction

Turbulent mass transfer across an air–water interface plays a critical role in geophysical and industrial processes. The basic problem in predicting the interfacial mass transfer is to estimate the mass transfer rate $K^*$ by using statistical properties of the velocity fields. Here, the mass transfer rate is defined as

$$K^* = \frac{Q^*}{\Delta\mu^*} = \frac{Q^*}{(\alpha \cdot C^*_{\mathrm{Ba}} - C^*_{\mathrm{Bw}})}, \tag{1}$$

where, $Q$, $\Delta\mu$, $C_{\mathrm{Ba}}$ and $C_{\mathrm{Bw}}$ are the mean interfacial mass flux, the chemical potential difference of a dissolved gas between air and water, and the bulk concentrations in the two phases, respectively. A value with an asterisk represents a dimensional value throughout this article, while $\alpha$ is the dimensionless Ostwald solubility, which is defined as the ratio of the equilibrium bulk concentrations in water and air $\alpha = C^*_{\mathrm{Bw}}/C^*_{\mathrm{Ba}}$.

The total mass transfer rate $K^*$ is represented by the respective mass transfer rates in the air and water phases, $K^*_{\mathrm{a}}$ and $K^*_{\mathrm{w}}$, as

$$K^* = \frac{K^*_{\mathrm{a}} K^*_{\mathrm{w}}}{K^*_{\mathrm{a}} + \alpha \cdot K^*_{\mathrm{w}}}. \tag{2}$$

In general, the molecular diffusivity in air $D^*_{\mathrm{a}}$ is much larger than that in water $D^*_{\mathrm{w}}$, so that, except for highly soluble ($\alpha \gg \mathrm{O}(1)$) or reactive gases, the most mass transfer resistance exists on the water side, i.e., $\alpha K^*_{\mathrm{w}} \ll K^*_{\mathrm{a}}$ or $K^* \sim K^*_{\mathrm{w}}$. Furthermore, since the Schmidt number $Sc$, which is defined by the ratio between the kinematic viscosity $\nu^*$ and the molecular diffusivity $D^*$, becomes extremely high $Sc_{\mathrm{w}} = \nu^*_{\mathrm{w}}/D^*_{\mathrm{w}} \sim \mathrm{O}(10^3)$ in water, a thin concentration boundary layer (10–100 μm) is formed just beneath the interface [1]. Therefore, it is particularly important to understand the microscopic transport mechanism inside this thin concentration boundary layer, which should be controlled by complex interaction between bulk turbulence, a free surface and waves.

However, due to difficulties in the measurement of velocity and concentration close to a moving interface, most efforts have been directed toward developing a correlation equation which relates the mass transfer rate to the macroscopic flow parameters. For example, empirical relationships between the mass transfer rate and wind velocity have been widely used to estimate the gas exchange across the sea surface in the field of geoscience [2]. In chemical engineering, an eddy-structure based model, i.e., the surface-renewal model [3], was proposed. In this model, the mass transfer rate is estimated from the surface-renewal time $\tau^*_{\mathrm{s}}$ as

$$K^*_{\mathrm{w}} \propto \sqrt{\frac{D^*_{\mathrm{w}}}{\tau^*_{\mathrm{s}}}}. \tag{3}$$

Different approaches have been proposed to determine the surface-renewal time, e.g., the large-eddy model [4], the small-eddy model [5,6] and the bursting-frequency model [7,8]. However, they do not

* Corresponding author. Tel.: +81 3 5841 6418; fax: +81 3 5800 6999.
*E-mail address:* hasegawa@thtlab.t.u-tokyo.ac.jp (Y. Hasegawa).

0017-9310/$ - see front matter © 2008 Elsevier Ltd. All rights reserved.
doi:10.1016/j.ijheatmasstransfer.2008.07.015

**Nomenclature**

| | |
|---|---|
| $A$ | dimensionless proportional constant in the surface divergence model |
| $c$ | concentration |
| $C$ | mean concentration |
| $C_c$ | Smagorinsky coefficient in the Dynamic Smagorinsky Model |
| $D$ | molecular diffusivity |
| $K$ | global mass transfer rate |
| $k$ | local mass transfer rate |
| $k_x$, $k_y$, $k_z$ | wavenumbers in the streamwise, interface-normal and spanwise directions |
| $k_{x\_LES}$, $k_{z\_LES}$ | maximum wavenumbers of Fourier modes in the streamwise and spanwise directions in LES region |
| $p$ | pressure |
| $Q$ | mean mass flux at the interface |
| $q$ | local mass flux at the interface |
| $R_{\alpha\beta}$ | correlation coefficient between variables $a$ and $b$ |
| $Re_\tau$ | Reynolds number based on the friction velocity $u_\tau$ and depth $\delta$ |
| $N$ | number of grid points |
| $Sc$ | Schmidt number |
| $t$ | time |
| $u$, $v$, $w$ | velocity components in the $x$, $y$, and $z$ directions |
| $u_\tau$ | friction velocity |
| $x$, $y$, $z$ | streamwise, interface-normal and spanwise directions |

*Greeks*

| | |
|---|---|
| $\alpha$ | dimensionless Ostwald solubility |
| $\beta$ | surface divergence |
| $\Delta C$ | difference between concentrations at the top and bottom boundaries |
| $\Delta C_B$ | difference between the bulk concentrations in air and water |
| $\Delta t$ | time step |
| $\Delta x$, $\Delta y$, $\Delta z$ | grid spacings in the streamwise, interface-normal and spanwise directions |
| $\delta$ | depth of computational domain |
| $\delta_B$ | thickness of the Batchelor sublayer |
| $\nu$ | kinematic viscosity |
| $\rho$ | fluid density |
| $\tau_s$ | surface-renewal time |
| $\omega$ | frequency |
| $\xi_i$ | subgrid-scale mass flux in the $i$th direction |

*Superscripts*

| | |
|---|---|
| $()^*$ | dimensional value |
| $()^+$ | value non-dimensionalized by the shear unit |
| $()'$ | fluctuating component |
| $\overline{()}$ | mean component |
| $\widehat{()}$ | Filtered value |
| $\widetilde{()}$ | Fourier coefficient |

*Subscripts*

| | |
|---|---|
| $()_a$ | value in air |
| $()_B$ | value in bulk |
| $()_I$ | value at the interface |
| $()_{rms}$ | root-mean-square value |
| $()_w$ | value in water |

have wide applicability, since they employ parameters that depend on a particular flow condition or turbulence properties in the bulk region away from the interface. For example, it is well known that the presence of surfactants causes strong attenuation of near-surface turbulence and also a drastic decease in the mass transfer rate [9]; this is quite difficult to predict only from bulk information.

In order to develop a general and robust model, a local parameter which governs the transport processes in the vicinity of the interface should be properly implemented into the model. Chan and Scriven [10] first shed light on a role of irrotational stagnation flow in the gas exchange across a free surface. They showed that the transport equation at a stagnation point reduces to

$$\frac{\partial c}{\partial t} + v\frac{\partial c}{\partial y} = \frac{1}{Sc}\frac{\partial^2 c}{\partial y^2}, \tag{4}$$

where $y$ is the distance from the interface and $v$ is the velocity in the $y$ direction. Since the concentration boundary layer is generally thinner than the viscous sublayer, $v$ can be approximated by the first term in a Taylor series as

$$v(y) - v(0) \sim -\left(\frac{\partial u}{\partial x} + \frac{\partial w}{\partial z}\right)_{y=0} \times y = -\beta y. \tag{5}$$

Here, $\beta$ is called the surface divergence.

Recently, particle image velocimetry (PIV) techniques have been successfully applied to the measurement of interfacial velocity fluctuations by several researchers. Their results indicate a possibility that the statistical properties of surface divergence can be related to the mass transfer rate regardless of a mode of turbulence generation [11,12], surface contamination [13] and interface deformation [14].

In the meantime, numerical simulations [15–17] have been performed to clarify the microscopic transport mechanisms at high Schmidt numbers. Basically, their data support the hypothesis that the surface divergence is the key parameter which governs the interfacial mass transfer. However, no literature discusses the quantitative relationship between the local mass transfer rate and the surface divergence, which is of critical importance to verify the surface divergence model. Furthermore, in the presence of the wind shear, which is of particular interest in the preset study, the interfacial shear stress determines turbulence structures in the water phase. Hence, the air–water coupling effects on the mass transfer must be clarified.

Main issues in the present study are as follows:

1. How the local interfacial mass transfer rate can be estimated when the surface divergence at a point of interest is specified?
2. What kind of conditions should be satisfied in order for the surface divergence to contribute to the mass transfer?
3. How the interaction between air and water turbulent flows influences the local interfacial mass transfer rate?

In order to calculate high Schmidt number concentration field, we employ a hybrid DNS/LES scheme [9,18], in which DNS with fine mesh is applied inside the thin concentration boundary layer, while LES with coarse mesh in the outer layer.

We will proceed as follows. In Section 2, we describe a computational model and numerical procedures of the hybrid DNS/LES scheme. In Section 3, we show fundamental concentration statistics in the air and water phases. Then, we study the interfacial mass transfer mechanisms with particular focus on air–water coupling effects. In Section 4, we revisit a one-dimensional advection–diffusion equation (4), and derive quantitative relationship between the local mass transfer rate and the surface divergence. Finally, we summarize the present study in Section 5.

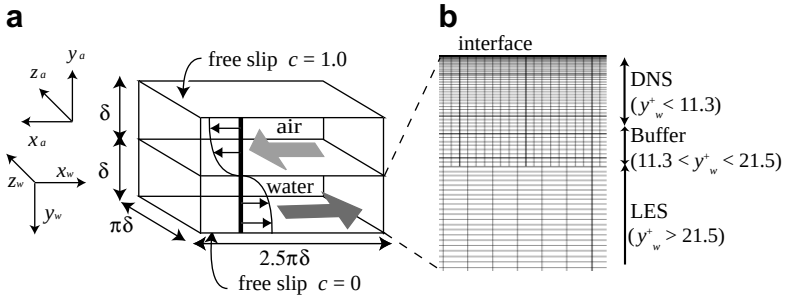


**Fig. 1.** (a) Computational domain, coordinate system and (b) grid system in the hybrid DNS/LES method.

## 2. Computational model

### 2.1. Numerical conditions

We consider a counter-current air–water flow driven by constant pressure gradient. The flow geometry and the coordinate system are shown in Fig. 1, where $x$, $y$ and $z$ are the streamwise, interface-normal and spanwise directions, respectively. The Reynolds numbers based on the interfacial friction velocity $u_\tau^*$ and the depth $\delta^*$ were set to be $Re_{\tau w} = Re_{\tau a} = 150$. The density ratio of water and air is $\rho_w^*/\rho_a^* = 841$.

The governing equations are the incompressible Navier–Stokes and the continuity equations,

$$\frac{\partial u_i}{\partial t} + u_j \frac{\partial u_i}{\partial x_j} = -\frac{\partial p}{\partial x_i} + \frac{1}{Re_\tau}\frac{\partial^2 u_i}{\partial x_j \partial x_j}, \tag{6}$$

$$\frac{\partial u_i}{\partial x_i} = 0, \tag{7}$$

where, the velocity $u_i$ and the coordinate $x_i$ are non-dimensionalized by $u_\tau^*$ and $\delta^*$ in each phase. A pseudo-spectral method with Fourier series in the $x$ and $z$ directions and a Chebyshev polynomials expansion in the $y$ direction was applied. Details of the numerical procedures are also described in Hasegawa and Kasagi [9,18]. Numbers of modes and grid spacings are listed in Table 1.

Since we focus on quantitative relationship between the local mass transfer rate and the surface divergence, the interface is assumed to be always flat for simplicity. Hence, the resultant coupling conditions at the air–water interface are the continuity of velocity and tangential shear stresses. They are rewritten in dimensionless forms as

$$u_{i_a} = \sqrt{\frac{\rho_a}{\rho_w}} u_{i_w} \quad (i = 1 \text{ or } 3), \tag{8}$$

$$u_{2_a} = u_{2_w} = 0, \tag{9}$$

$$\frac{1}{Re_{\tau a}}\frac{\partial u_{i_a}}{\partial x_{2_a}} = \frac{1}{Re_{\tau w}}\frac{\partial u_{i_w}}{\partial x_{2_w}} \quad (i = 1 \text{ or } 3). \tag{10}$$

Once the velocity field is calculated at each time step, the concentration field of a dissolved gas is obtained by integrating the following transport equation.

$$\frac{\partial c}{\partial t} + u_j \frac{\partial c}{\partial x_j} = \frac{1}{Re_\tau \cdot Sc}\frac{\partial^2 c}{\partial x_j \partial x_j}. \tag{11}$$

The dimensionless concentrations in the air and water phases are defined as

$$c_a = \frac{\alpha \cdot c_a^* - c_{w_{bottom}}^*}{\alpha \cdot c_{a_{top}}^* - c_{w_{bottom}}^*}, \tag{12}$$

$$c_w = \frac{c_w^* - c_{w_{bottom}}^*}{\alpha \cdot c_{a_{top}}^* - c_{w_{bottom}}^*}. \tag{13}$$

Here, $\alpha c_a^*$ is the equivalent molar concentration in water at equilibrium, when the molar concentration of a gaseous solute in air is $c_a^*$. In Eqs. (12) and (13), $c_{a_{top}}^*$ and $c_{w_{bottom}}^*$ are the molar concentrations at the outer boundaries in air and water phases, respectively. At the interface, the following Henry's law and the continuity of mass flux are employed so that

$$c_a = c_w, \tag{14}$$

$$\frac{\partial c_a}{\partial y_a} = -\alpha \frac{Sc_a Re_{\tau a}}{Sc_w Re_{\tau w}} \sqrt{\frac{\rho_a}{\rho_w}} \frac{\partial c_w}{\partial y_w}. \tag{15}$$

**Table 1**
Computational conditions (number of modes, number of grid points and grid spacings)

| | | Region | $k_x$, $k_y$ or $N_y$, $k_z$ | $\Delta x^+$ | $\Delta y^+$ | $\Delta z^+$ |
|---|---|---|---|---|---|---|
| Velocity | DNS | $0 < y^+ < 150$ | 64, 129, 64 | 18.4 | 0.01–1.23 | 7.2 |
| Case 1 | DNS | $0 < y^+ < 11.3$ | 192, 34, 192 | 6.1 | 0.01–0.62 | 2.4 |
| | Switching | $11.3 < y^+ < 21.6$ | 192, 15, 192 | 6.1 | 0.66–0.85 | 2.4 |
| | LES | $21.6 < y^+ < 150$ | 64, 144, 64 | 18.4 | 0.86–1.23 | 7.2 |
| Case 2 | DNS | $0 < y^+ < 22.8$ | 192, 50, 192 | 6.1 | 0.01–0.79 | 2.4 |
| | Switching | $22.8 < y^+ < 35.4$ | 192, 15, 192 | 6.1 | 0.81–0.85 | 2.4 |
| | LES | $35.4 < y^+ < 150$ | 64, 128, 64 | 18.4 | 0.86–1.23 | 7.2 |
| Velocity | DNS | $0 < y^+ < 150$ | 64, 289, 64 | 18.4 | 0.002–0.38 | 7.2 |
| Case 3 | DNS | $0 < y^+ < 16.5$ | 512, 94, 512 | 2.3 | 0.002–0.34 | 0.9 |
| | Switching | $16.5 < y^+ < 21.6$ | 512, 15, 512 | 2.3 | 0.35–0.38 | 0.9 |
| | LES | $21.6 < y^+ < 150$ | 64, 324, 64 | 18.4 | 0.002–0.38 | 7.2 |
| Velocity | DNS | $0 < y^+ < 150$ | 96, 129, 96 | 12.3 | 0.01–1.23 | 4.9 |
| Case 4 | DNS | $0 < y^+ < 11.3$ | 192, 34, 192 | 6.1 | 0.01–0.62 | 2.4 |
| | Switching | $11.3 < y^+ < 21.6$ | 192, 15, 192 | 6.1 | 0.66–0.85 | 2.4 |
| | LES | $21.6 < y^+ < 150$ | 96, 144, 96 | 12.3 | 0.86–1.23 | 4.9 |

In this work, $\alpha$ is assumed 1.0, which approximately corresponds to the solubility of carbon dioxide at the standard temperature and pressure.

The Schmidt numbers used in this study are 1.0 and 100 in water, while kept constant at $Sc_a = 1.0$ in air. DNS is applied to the concentration field at $Sc_w = 1.0$ in the whole domain by using a pseudo-spectral method. For the high Schmidt number of 100, the hybrid DNS/LES scheme is employed.

### 2.2. Hybrid DNS/LES scheme

In the hybrid DNS/LES scheme, the computational domain in water is divided into three regions, i.e., DNS, switching and LES regions, as shown in Fig. 1b. The depth of the DNS region is determined so that more than 95% of the mean concentration change is resolved by DNS. In order to connect the DNS and LES regions smoothly, we provide the switching region between them.

For spatial discretization, Fourier series are used in the $x$ and $z$ directions, and the finite volume method is employed in the $y$ direction. In the DNS and switching regions, Fourier modes up to 8 times that for the velocity field are employed in the $x$ and $z$ directions, whereas in the LES region, the same grid system as that for the velocity field is used.

In the present study, the grid resolution in the air phase is the same as that for the velocity field in the water phase (or the concentration field in the LES region). The concentration fields in the air and water phases at low wavenumbers $|k_x| \leqslant k_{x\_LES}$ and $|k_z| \leqslant k_{z\_LES}$ are coupled through the Henry's law and the continuity of mass flux given by Eqs. (14) and (15), respectively. Here, $k_{x\_LES}$ and $k_{z\_LES}$ are the maximum wavenumbers in $x$ and $z$ directions in the LES region. For higher wavenumbers, $\tilde{c}(k_x, 0, k_z) = 0$ is imposed at the interface, where $\tilde{c}(k_x, y, k_z)$ denotes a Fourier coefficient of concentration fluctuation for the streamwise and spanwise wavenumbers of $k_x$ and $k_z$ at the $x$-$z$ plane a distance $y$ from the interface.

The filtered transport equation for concentration $c$ can be given as

$$\frac{\partial \widehat{c}}{\partial t} + \widehat{u}_j \frac{\partial \widehat{c}}{\partial x_j} = \frac{1}{Re_\tau \cdot Sc} \frac{\partial^2 \widehat{c}}{\partial x_j \partial x_j} - \frac{\partial (A_c \xi_j)}{\partial x_j}. \tag{16}$$

where $\xi_j$ is the subgrid-scale mass flux. For the subgrid model, we employed the Dynamic Smagorinsky Model (DSM):

$$\xi_j = -2C_c \widehat{\Delta}^2 |\widehat{S_{ij}}| \frac{\partial \widehat{c}}{\partial x_j}. \tag{17}$$

where $\widehat{\Delta}$ and $\widehat{S_{ij}}$ denote the local grid width and the strain rate tensor, respectively. The unknown coefficient $C_c$ is calculated using the Germano identity with the double-filtering procedure [19]. In Eq. (16), $A_c$ is a function of the distance from the interface $y_w$ and acts as a switching function between DNS and LES. In the DNS and LES regions, $A_c$ takes two limiting values of 0 and 1, respectively. In the switching region, $A_c$ is linearly increased from 0 to 1 with the distance from the interface.

In order to verify the present calculation, we run four computations with different depths of the DNS region (Cases 1 and 2) and different grid resolutions for the concentration and velocity fields (Cases 1, 3 and 4). All computational conditions are listed in Table 1. The verification procedures are essentially the same as those in Hasegawa and Kasagi [18].

## 3. High Schmidt number effects on concentration field

### 3.1. Statistics of concentration field

The flow statistics under the present condition have been already reported by Lombardi et al. [20]. They also mentioned that

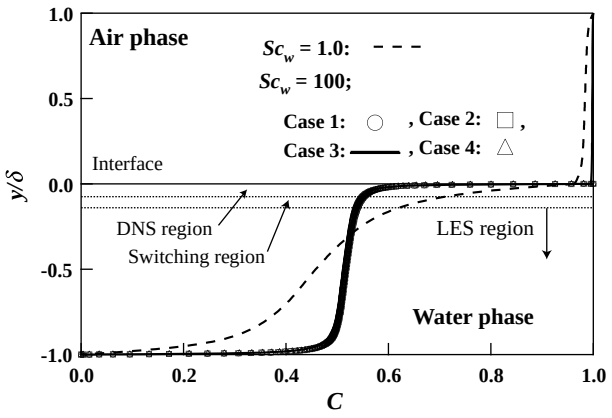


**Fig. 2.** Mean concentration profile.

20% of quasi-streamwise vortices appeared to be coupled across the interface. However, the air–water coupling was found to be too weak for the detection technique they used, so that the presence of the coupling and its effects on the interfacial mass transfer still remain open questions. In this section, we focus on the coupling effects on the concentration statistics and the mass transfer mechanisms.

The mean concentration profile in the air and water phases is presented in Fig. 2. Due to the large density ratio in Eq. (15), the most mass transfer resistance exists in the water phase, even though the Schmidt numbers in both phases are the same, i.e., $Sc_w = Sc_a = 1.0$. With increasing $Sc_w$ from 1 to 100, the resistance in water is more pronounced. Namely, the interfacial mean con-

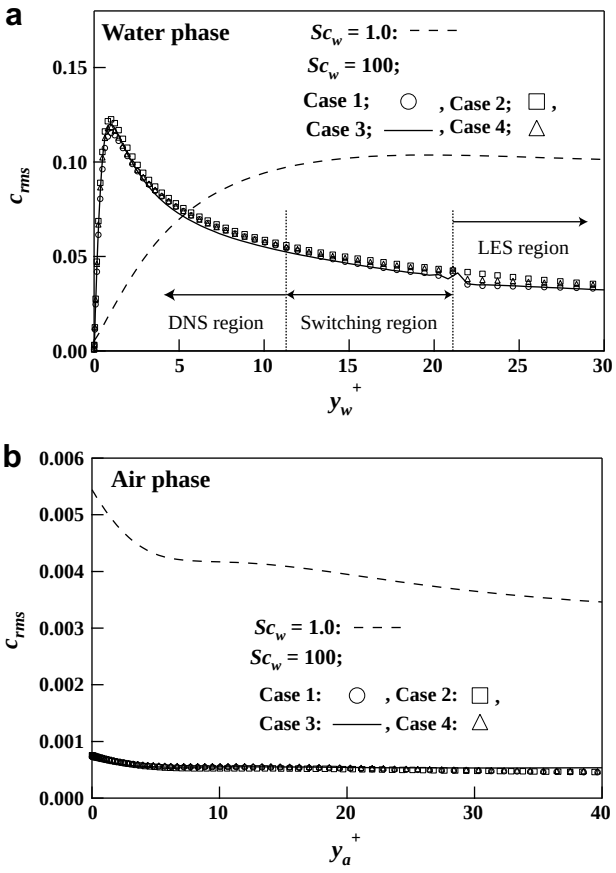


**Fig. 3.** Concentration fluctuation in (a) water and (b) air phases.

centrations at $Sc_w = 1.0$ and 100 are $C_I = 0.964$ and 0.995, respectively. The boundaries between the DNS, switching and LES regions in Case 1 are also depicted in Fig. 2. By inserting the switching region, we obtain the smooth profile across the boundaries.

The concentration fluctuations close to the interface in the water and air phases are shown in Fig. 3a and b, respectively. Since the most concentration change occurs in the water phase, the concentration fluctuation $c_{rms}(y = 0)$ at the interface is negligible for the aqueous concentration boundary layer. With increasing the Schmidt number in water, the interfacial concentration fluctuation is further decreased. Specifically, $c_{rms}(y = 0) = 0.54 \times 10^{-2}$ and $0.73 \times 10^{-3}$ at $Sc_w = 1.0$ and 100, respectively. The peak value of the concentration fluctuation normalized by the difference $\Delta C_{Bw}$ between the interfacial concentration and bulk concentrations in water is about 0.25 at $Sc_w = 100$, which agrees well with the LES data of Calmet and Magnaudet [16].

In the air phase, the concentration fluctuation has its peak at the interface (see Fig. 3b). This indicates that the concentration fluctuation generated in water is transported across the interface by molecular diffusion as will be discussed in Section 3.2. The generation of concentration fluctuation in air is insignificant because the mean concentration gradient is much smaller than that in water.

In Figs. 2 and 3, the results in Cases 1–4 are plotted. It is found that the dependency on the grid resolution and the depth of the DNS region is quite weak. Specifically, the difference in the mass transfer rate $K$ is less than 2%. Hanratty [21] complied experimental data under a wide range of the Reynolds number and concluded that $K$ can be well expressed in the simple form as $K^+ = K^*/u^*_{\tau w} = BSc_w^{-1/2}$, where the proportional constant $B$ is around 0.12. Jähne et al. [22] obtained $B = 0.11$ from experiments in circular and linear wind/wave tunnels with various tracers. The value of $B$ obtained in the present calculation is 0.097, which agrees fairly well with the experimental data. The slight underestimate in the present study might be attributed to the neglect of surface waves, since DNS data for a deformable sheared interface [15] results in a slightly higher value of $B = 0.11$. We should also note that the effects of the bottom wall are also included in the experimental data.

We also confirmed that the one-dimensional spectra of concentration fluctuation in the $x$ and $z$ directions show good agreement over the whole range of wavenumbers in all cases. The concentration spectra close to free and solid surfaces at different resolutions were reported in Hasegawa and Kasagi [18]. In order to clarify the effects of grid refinement in the $x$ and $z$ directions, we performed additional calculation without horizontal gird refinement. In this case, the concentration fluctuations at high wavenumbers significantly accumulate so that the concentration fluctuation is overestimated by 5% around the peak location. From these results, we conclude that the grid resolution and the depth of the DNS region used in Case 1 are necessary and sufficient not only to obtain the concentration statistics, but also to study the local mass transfer mechanisms. Hereafter, the results obtained in Case 1 is shown.

### 3.2. Spatio-temporal correlation between local mass transfer rate and velocity components

In order to clarify air–water coupling effects on the interfacial mass transfer, the following spatio-temporal correlation coefficients between the local mass transfer rate $k$, and velocity/concentration fluctuations around the interface are calculated:

$$R_{k\gamma}(y, \Delta t) = \frac{\overline{k'(x,z,t) \cdot \gamma'(x,y,z,t+\Delta t)}}{k_{rms} \cdot \gamma_{rms}}, \tag{18}$$

where,

$$k = \frac{q^*}{u^*_{\tau w} \cdot \Delta C^*} = \frac{-1}{Sc_w \cdot Re_{\tau w}} \frac{\partial c_w}{\partial y_w}|_{y_w=0}, \tag{19}$$

and $\gamma$ in Eq. (18) represents a velocity component or concentration. In calculating the spatio-temporal correlation, $x$ is directed to the air flow direction, while $y$ is distance from the interface defined to be positive in air and negative in water. The results at $Sc_w = 1.0$ and 100 are shown in Fig. 4a and b, respectively.

In general, the spatio-temporal correlations have larger absolute values on the water side. Specifically, upwelling of low concentration fluid leads to high mass transfer rate ($R_{kv} > 0$, $R_{kc} < 0$). With increasing the Schmidt number from 1.0 to 100, the absolute values of $R_{ku}$ and $R_{kc}$ are decreased away from the interface, i.e., $y^+_w = 7.2$. In contrast, $R_{kv}$ is kept high, i.e., $R_{kv} \sim 0.6$ even at the high Schmidt number. This suggests that the normal velocity fluctuation plays a critical role in controlling the local mass flux.

In the air phase, $R_{kc}$ shows a considerable value close to the interface. Specifically, negative concentration fluctuation ($R_{kc} < 0$) is associated with high interfacial mass flux. It is diffused inside the air phase with time. This result indicates that impingement of low concentration water on the interface governs the concentration fluctuation in air. This is consistent with the fact that the concentration fluctuation in the air phase has a peak at the interface as shown in Fig. 3b. In contrast, the correlation between $k$ and velocity components are generally quite small. This indicates that the velocity fluctuation in the air phase hardly contributes to the interfacial mass transfer. This agrees with wind-tunnel measurements by Komori et al. [23], where the frequency of the appearance of organized turbulent motions in water is found to be much lower than that in air at the low wind speed considered here. Hanratty [21] estimated the normal velocity fluctuations in water induced by the fluctuating wind shear as

$$\lim_{y_w \to 0} (v^+_w)_{rms} = (\tau^+_z)_{rms} \sqrt{\frac{\rho_a}{\rho_w}} \frac{Re_{\tau a}}{Re_{\tau w}} \frac{\pi}{\sqrt{\omega^+_a}\lambda^+_a} y^+_w, \tag{20}$$

Here, $\lambda^+_a$ and $\sqrt{\omega^+_a}$ is typical diameter and frequency of quasi-streamwise vortices in the air phase. $\tau^+_z$ is the spanwise interfacial shear stress associated with the quasi-streamwseise vortices. Assuming that $\lambda^+_a = 20$, $\omega^+_a = 0.1$ and $(\tau^+_z)_{rms} = 0.1$, Eq. (20) leads to $\lim_{y_w \to 0}(v^+_w)_{rms} \sim 0.002 y^+_w$. This value is at most 3% of the present numerical result. Hence, we conclude that the self-sustaining mechanisms of turbulence due to the mean shear, which are similar to those near a solid wall, are dominant in water. Hereafter, we focus on turbulent transports in the water phase.

### 3.3. Visualization of velocity and concentration fields near interface

The instantaneous distributions of the local mass transfer rate $k$ at $Sc_w = 1.0$ and 100 under the identical flow field are shown in Fig. 5a and b, respectively. Low mass-flux regions have streaky structures. They become finer with the Schmidt number increased. On the other hand, high mass-flux regions are characterized by spotty structures. These structures are almost independent of the Schmidt number and even more highlighted at $Sc_w = 100$.

In order to investigate the relationship between the high mass-flux regions and turbulent structures, the instantaneous velocity vectors and concentration fluctuation in the $y$–$z$ plane are presented in Fig. 6. The local mass transfer rate $k$, the surface divergence $\beta$ and the fluctuation component of streamwise interfacial shear stress $\tau'_x$ are also plotted. It is observed that the local mass transfer rate correlates with the surface divergence fairly well even at the high Schmidt number. In contrast, the local shear stress is poorly correlated with any of them. This is consistent with high $R_{kv}$ in Fig. 4b.

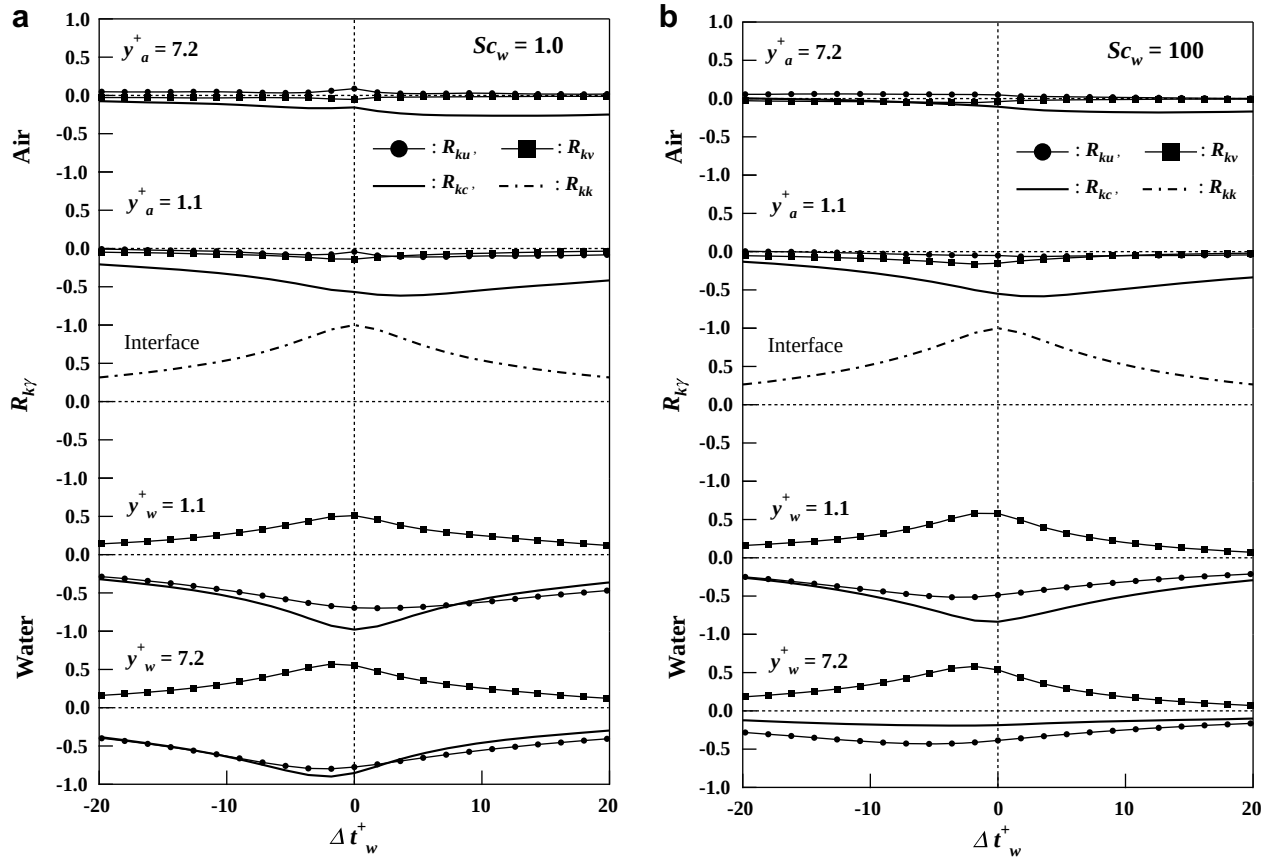


**Fig. 4.** Spatio-temporal correlation between local mass transfer rate and velocity/concentration fluctuations close to the interface at (a) $Sc_w$ = 1.0 and (b) $Sc_w$ = 100.

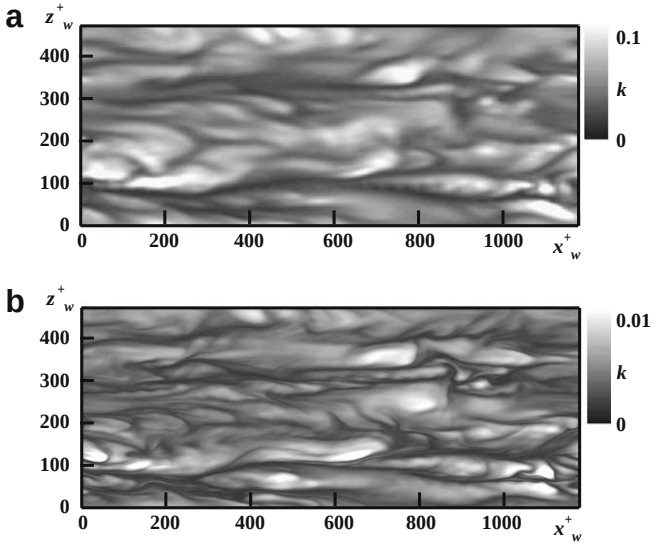


**Fig. 5.** Local mass transfer rate at (a) $Sc_w$ = 1.0 and (b) $Sc_w$ = 100.

The high surface divergence region is caused by upwelling flow associated with the streamwise vortex beneath the interface (see Fig. 6b). This upwelling flow carries fresh fluid from the LES region to the DNS region and brings about a large interfacial mass flux, so the adequate coupling between the concentration fields calculated by DNS and LES is important.

## 4. Interfacial mass transfer model

### 4.1. One-dimensional advection–diffusion equation

In order to investigate the quantitative relationship between the local mass transfer rate and the surface divergence, a one-dimensional advection–diffusion equation in the water phase is revisited. Chan and Scriven [10] showed that the transport equation in an irrotational stagnation flow reduces without approximation to

$$\frac{\partial c}{\partial t^+} - \beta^+(t) y^+ \cdot \frac{\partial c}{\partial y^+} = \frac{1}{Sc} \cdot \frac{\partial^2 c}{\partial y^{+2}}, \tag{21}$$

where the velocity and the length are non-dimensionalized by the shear units on the water side. The concentration is normalized by the concentration difference $\Delta C^*_{B_w}$ between the interface and the bulk in water. Following McCready et al. [24], the fluctuating surface divergence is modelled as

$$\beta^+(t) = \sqrt{2}\beta^+_0 \cos(\omega^+_0 t^+), \tag{22}$$

where $\beta^+_0 = \beta^+_{rms} = \sqrt{\overline{(-\partial v^+/\partial y^+|_{y^+=0})^2}}$.

If we introduce a new coordinate $Y = \sqrt{Sc\omega^+_0} y^+$ and a time-scale $T = \omega^+_0 t^+$, the Schmidt number disappears from Eq. (21), and the only remaining parameter is $\beta^+_0/\omega^+_0$ as follows:

$$\frac{\partial c}{\partial T} - \sqrt{2}\frac{\beta^+_0}{\omega^+_0} \cos(T) \cdot Y \cdot \frac{\partial c}{\partial Y} = \frac{\partial^2 c}{\partial Y^2}. \tag{23}$$

Since the concentration profile obtained by Eq. (23) continues to grow, following Brumley and Jirka [25], we assume a length-scale $L^+$, beyond which turbulence always completely mixes the dissolved

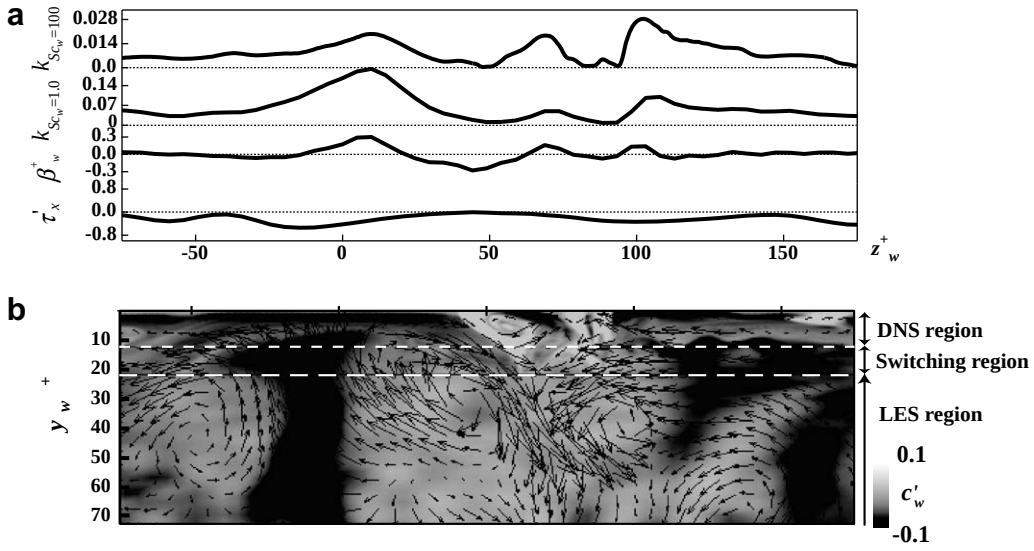


**Fig. 6.** (a) Local mass transfer rate $k$ at $Sc_w = 1.0$ and 100, surface divergence $\beta_w^+$ and interfacial streamwise shear stress fluctuation $\tau_x'$. (b) Concentration and velocity fluctuations in the $y$–$z$ plane.

gas. Specifically, the tail of the concentration boundary layer is instantaneously chopped off in the region of $y^+ > L^+$, (i.e., $Y > L = \sqrt{Sc\omega_0^+}L^+$) whenever the normal velocity fluctuation switches from downwelling to upwelling.

In the above model, the Schmidt number appears only in the distance $L = \sqrt{Sc\omega_0^+}L^+$ between the interface and the outer boundary. By assuming $L^+ = 2$, and $\omega_0^+ = 0.1$, which represents the thickness of the viscous sublayer and the typical frequency of the surface divergence, respectively, we find that $L$ changes within the range of $O(1) < L < O(10)$ when $Sc$ is increased from 1.0 to 100. Fortunately, the influence of $L$ on the solution of Eq. (23) is found quite weak. Therefore, we fix $L = 50$ and focus on the effect of $\beta_0^+/\omega_0^+$ on the solution.

The mass transfer rate $K_w^+$ and the correlation coefficient $R_{cv}$ at the interface obtained from Eq. (23) are presented in Fig. 7. It is found that the solution of Eq. (23) undergoes a sudden transition around $\beta_0^+/\omega_0^+ = 1$. Specifically, when $\beta_0^+/\omega_0^+ > 10$, $R_{cv}$ is kept high and $K_w^+$ is proportional to $\sqrt{\beta_0^+/Sc}$. In contrast, when $\beta_0^+/\omega_0^+ < 1$, both $K_w^+$ and $R_{cv}$ are decreased drastically. In the following subsection, we will look into the transport mechanism in the two typical regimes by focusing on two time-scales characterizing the concentration filed near the interface.

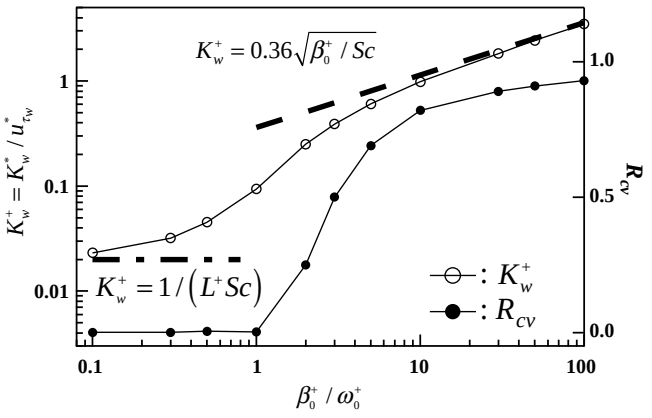


**Fig. 7.** Mass transfer rate $K_w^+$ and correlation coefficient $R_{cv}$ between velocity and concentration fluctuations at the interface when $L = \sqrt{Sc\omega_0^+}L^+ = 50$.

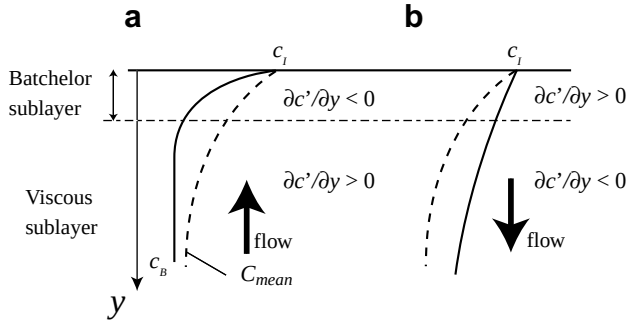


**Fig. 8.** Mechanism of $\overline{c_w' v_w'}$ generation due to the normal straining motion near the interface in the cases of (a) upwelling flow $\beta = -\partial v/\partial y|_{y=0} > 0$ and (b) downwelling flow $\beta = -\partial v/\partial y|_{y=0} < 0$.

### 4.2. Response and renewal time-scales

According to the Chan and Scriven's result [10] for steady upwelling flow, i.e., $\beta^+ = \text{const.}$ and positive (see Fig. 8a), the transient response time of the concentration field scales with $1/\beta^+$ regardless of the Schmidt number. After the transient response time passes ($t^+ > 1/\beta^+$), the advection term balances with the diffusion term in Eq. (21). Hence, we call $1/\beta^+$ the response time-scale, which represents time for the concentration boundary layer to response to the surface divergence. In this case, the local mass transfer rate $k_{B_w}$ can be calculated analytically as

$$k_{B_w} = \frac{q^*}{u_\tau^* \Delta C_{B_w}^*} = \sqrt{\frac{2\beta^+}{\pi \cdot Sc}}. \tag{24}$$

Here, the typical length-scale of the concentration boundary layer is given by $\delta_B^+ \sim (\beta^+ Sc)^{-1/2}$. This length is similar to the Batchelor length-scale [26], which describes the smallest scale of concentration fluctuation in isotropic turbulence, if $\beta^+$ is taken as the typical intensity of straining motion. Therefore, we call this concentration boundary layer the Batchelor sublayer. Conversely, if $\beta^+$ is negative, i.e., in the case of flow away from the interface (see Fig. 8b), the concentration boundary layer is stretched exponentially with time, so that $k_{B_w}$ rapidly diminishes.

In the case of the fluctuating surface divergence given by Eq. (22), the renewal time-scale $1/\omega_0^+$, which is the typical time-scale of a period of the velocity fluctuation, newly appears. If the renewal time-scale $1/\omega_0^+$ is sufficiently larger than the response time-scale $1/\beta_0^+$, i.e., $\beta_0^+/\omega_0^+ \gg 1$, $k_{B_w}$ can be estimated as follows:

$$k_{B_w} = \frac{q^*}{u_{\tau w}\cdot \Delta C^*_{B_w}} = \begin{cases} \sqrt{\frac{2\beta^+}{\pi\cdot Sc}} \sim 0.8\sqrt{\frac{\beta^+}{Sc}} & \beta^+ > 0 \\ 0 & \beta^+ < 0. \end{cases} \tag{25}$$

The balance between the advection and diffusion terms can also be predicted independently from the above analysis by the decomposition of $c = C + c'$ and an order-of-magnitude estimation of the fluctuating term in Eq. (21):

$$\underbrace{\frac{\partial c'}{\partial t^+}}_{O(\omega_0^+ c')} \underbrace{- \beta^+(t) y^+ \frac{dC}{dy^+} + \overline{\beta^+(t) y^+ \frac{\partial c'}{\partial y^+}}}_{O(\beta_0^+ \delta_c \Delta C/\delta_c) = O(\beta_0^+ \Delta C)} = \underbrace{\frac{1}{Sc}\frac{\partial^2 c'}{\partial y^{+2}}}_{O(c'/(Sc\delta_c^2))} \tag{26}$$

Here, $\delta_c$ is the thickness of the concentration boundary layer. Since the scale of the concentration fluctuation $c'$ is at most $\Delta C$, the advection term must balance with the diffusion term when $\beta_0^+/\omega_0^+ \gg 1$.

Hence, when $\beta_0^+/\omega_0^+ \gg 1$, the concentration fluctuation is in phase with the velocity fluctuation ($R_{cv} \sim 1$) and the global mass transfer rate is correlated with the intensity of the surface divergence as

$$K_w^+ = \frac{K_w^*}{u_{\tau_w}^*} = A\sqrt{\frac{\beta_0^+}{Sc}}. \tag{27}$$

where the dimensionless proportional constant $A$ is 0.36 (see Fig. 7).

On the other hand, when $\beta_0^+/\omega_0^+ < 1$, the velocity fluctuates so frequently that the balance between the advection and diffusion terms does not hold anymore. Instead, the transient and advection terms become dominant throughout the concentration boundary layer. In this case, the transport Eq. (21) is approximated by

$$\frac{\partial c'}{\partial t^+} - \beta^+(t^+) y^+ \frac{dC}{dy^+} \sim 0. \tag{28}$$

By substituting $c'(y^+, t^+) = \tilde{c}(y^+)\cdot \exp(i\omega_0^+ t^+)$ and $\beta^+(t^+) = \tilde{\beta}\cdot \exp(i\omega_0^+ t^+)$, we obtain

$$\tilde{c}(y^+) = \frac{\tilde{\beta}}{i\omega_0^+}\frac{dC^+}{dy^+} y^+. \tag{29}$$

Eq. (29) indicates that the velocity fluctuation is out of phase with the concentration fluctuation by 90 deg, and therefore does not contribute to the mass transfer. This explains the drastic decrease of $R_{cv}$ and $K_w$ in Fig. 7 when $\beta_0^+/\omega_0^+ < 1$. In this case, the mass transfer rate converges to the value predicted by the film model [27], i.e., $K_w^+ = 1/(ScL^+)$ (see Fig. 7).

We confirmed that the balance of the fluctuating three terms in Eq. (21) switches from one of the above-mentioned two to the other in the neighborhood of $\beta_0^+/\omega_0^+ = 1$. As a result, the mass transfer mechanism drastically changes as shown in Fig. 7. Hence, we can conclude that the surface divergence contributes to the mass transfer only when $\beta_0^+/\omega_0^+ > 1$. In this case, the local mass transfer rate $k$ can be predicted by using the local surface divergence $\beta^+$ given by Eq. (25).

### 4.3. Quantitative relationship between local mass transfer rate and surface divergence

The contribution of the surface divergence $\beta^+$ to the interfacial mass flux at $Sc_w = 100$ obtained in the present calculation is shown in Fig. 9a. The contour value represents the product of the local mass transfer rate $k^+$ and the joint probability density function of $\beta^+$ and $k^+$, so that the integral of the contour value over the whole $\beta^+$–$k^+$ plane is identical to the total interfacial mass flux. The most interfacial mass flux occurs in the region of $\beta > 0$, and the contour shows good agreement with the prediction (25), which is depicted as a solid line.

In order to demonstrate the robustness of the surface divergence model (25), we conduct an additional calculation for high Schmidt number turbulent mass transfer across a shear-free interface. Upwelling and downwelling motions at a sheared interface are driven by streamwise vortices as shown in Fig. 6. In contrast, at a shear-free interface, they result from the distortion of bulk turbulence due to the interfacial blocking effects [28,29]. For these reasons, sheared and shear-free interfaces are sometimes referred to "active" and "passive" interfaces, respectively.

We consider an open channel flow, where a shear-free boundary condition is imposed for the tangential velocity components at the interface, while a no-slip condition for the bottom boundary. The interface is kept flat like the sheared case. The Reynolds number based on the friction velocity $u_\tau$ at the bottom wall and the depth $\delta$ is set to be $Re_\tau = 150$. The constant concentration conditions are imposed at the interface and the bottom wall, i.e., $c = 1$ and 0, respectively. The computational method and grids used for solving the high Schmidt number concentration filed are essentially the same as those used for the sheared interface.

In Fig. 9b, the contribution of the surface divergence to the interfacial mass flux at $Sc_w = 100$ at a shear-free interface is shown. Again, the present result agrees with the surface divergence model (25). It is worth noting that the data at a shear-free interface exhibits better agreement than those at a sheared interface. One sensible explanation for this would be the difference in the frequency range of the surface divergence fluctuation between the two interfaces. As discussed in Section 4.2, the time-scale ratio $\beta_0^+/\omega_0^+$ is considered as the effectiveness indicator of the surface divergence in the mass transfer. It is possible that the typical frequency of the surface divergence at a shear-free interface is lower than that at a sheared interface, so that the resultant effectiveness of the surface divergence is enhanced.

In summary, the present results indicate that Eq. (25) is quite robust regardless of the presence of the interfacial shear.

### 4.4. Budget of normal turbulent mass flux

The importance of the normal velocity fluctuation in the interfacial mass transfer is also highlighted in the budget equation for the interface-normal turbulent mass fluxes $\overline{c_w^{+\prime} v_w^{+\prime}}$ in the water phase given by

$$\frac{D\overline{(c^{+\prime}v^{+\prime})}}{Dt^+} = \underbrace{-\overline{v^{+2}}\frac{\partial C^+}{\partial y^+}}_{\text{Production}} \underbrace{- \frac{\partial \overline{c^{+\prime}v^{+\prime}v^{+\prime}}}{\partial y}}_{\text{Turbulent diffusion}} \underbrace{+ \frac{\partial}{\partial y}\left\{\overline{c^{+\prime}\frac{\partial v^{+\prime}}{\partial y^+}} + \frac{1}{Sc}\overline{v^{+\prime}\frac{\partial c^{+\prime}}{\partial y^+}}\right\}}_{\text{Molecular diffusion}}$$
$$\underbrace{- \overline{c^{+\prime}\cdot\frac{\partial p^{+\prime}}{\partial y^+}}}_{\text{Concentration pressure–gradient correlation}} \underbrace{- \left(1+\frac{1}{Sc}\right)\cdot\overline{\frac{\partial c^{+\prime}}{\partial x_j^+}\cdot\frac{\partial v^{+\prime}}{\partial x_j^+}}}_{\text{Dissipation}}. \tag{30}$$

Each term of Eq. (30) is shown in Fig. 10a and b. At $Sc_w = 1.0$, the production balances with the concentration pressure-gradient correlation away from the interface. The dissipation and molecular diffusion is generally very small except in the diffusive sublayer. On the other hand, at $Sc_w = 100$, the dissipation as well as the molecular diffusion becomes more dominant. An interesting feature is that the sign of the dissipation turns opposite where the sign of the molecular diffusion also changes. This trend is also found in the DNS data

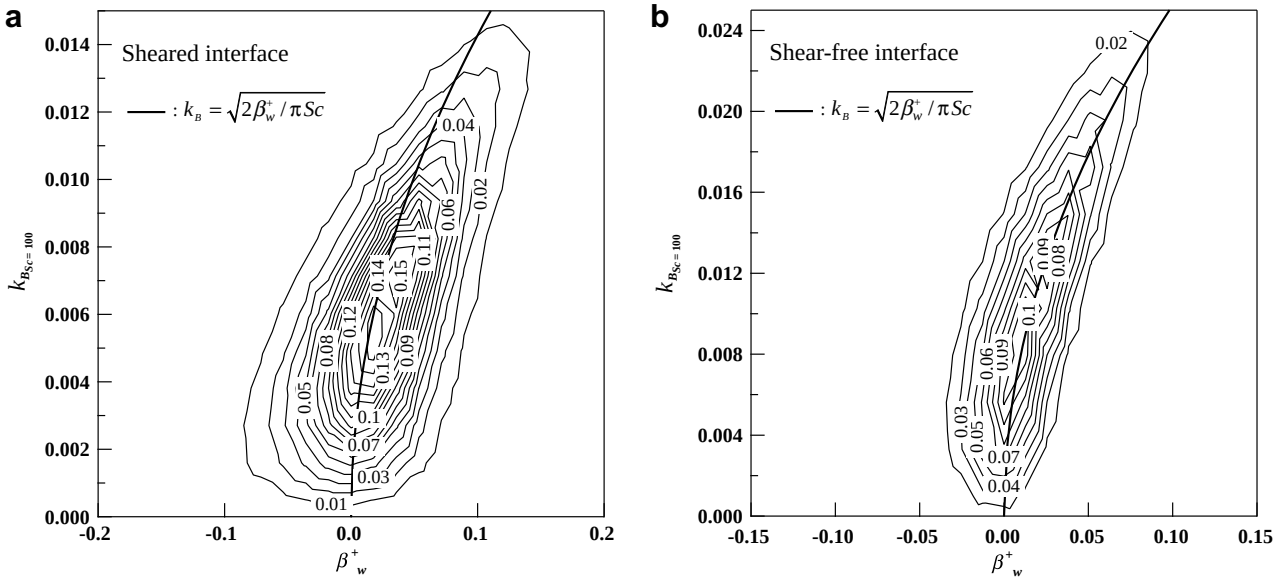


**Fig. 9.** Contribution of the surface divergence $\beta_w^+$ to local mass transfer rate $k_B$ at (a) sheared and (b) shear-free interfaces.

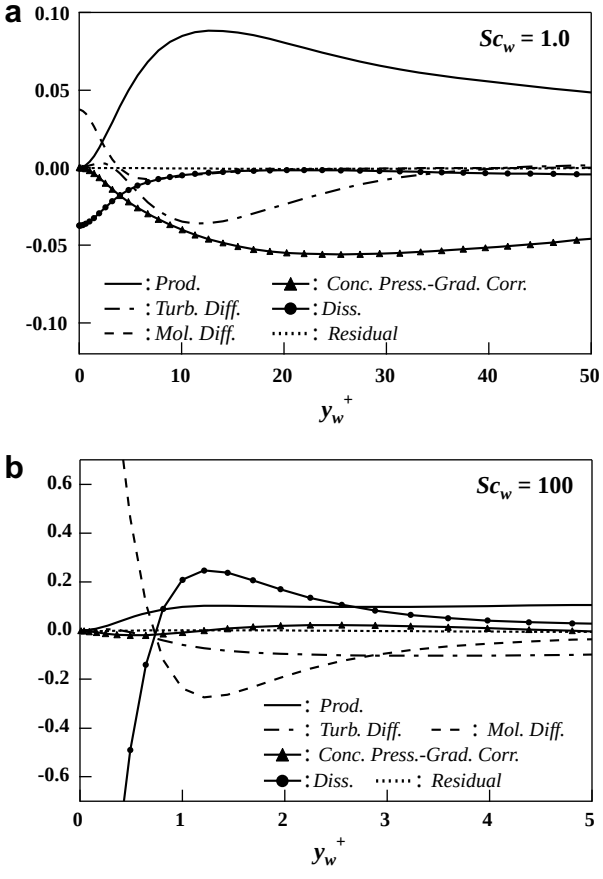


**Fig. 10.** Budget of the normal turbulent mass flux $\overline{c'_w v'_w}$ at (a) $Sc_w = 1.0$, (b) $Sc_w = 100$.

of Kawamura et al. [30] and Lakehal et al. [31] at moderate Schmidt numbers up to 10. As a result, the dissipation becomes a major source term in the region of $y_w^+ > 1$. By decomposing the dissipation term $-(1+Sc^{-1}) \cdot \overline{(\partial c'/\partial x_j)(\partial v'/\partial x_j)}$ into three directional components, it is found that the component in the $y$ direction $-(1+Sc^{-1}) \cdot \overline{(\partial c'/\partial y)(\partial v'/\partial y)}$ is dominant among the three (not shown here).

The above facts can be explained by a conceptual figure shown in Fig. 8. Since we consider the concentration field inside the viscous sublayer, we assume that $\partial v'/\partial y$ is nearly constant in this region. When an upwelling flow occurs, i.e., $\partial v'/\partial y < 0$, the concentration gradient becomes steeper than the mean concentration gradient inside the Batchelor sublayer, i.e., $\partial c'/\partial y < 0$, while flatter outside the Batchelor sublayer, i.e., $\partial c'/\partial y > 0$ (see Fig. 8a). Therefore, the dissipation of $\overline{c_w^{+\prime} v_w^{+\prime}}$ turns positive outside the Batchelor sublayer. On the other hand, in the case of a downwelling flow, i.e., $\partial v'/\partial y > 0$, the concentration profile is stretched downward, and the sign of $\partial c'/\partial y$ becomes positive close to the interface, while negative far from the interface (see Fig. 8b). As a result, the dissipation rate becomes positive outside the Bachelor sublayer in both cases.

According to the above consideration, the dissipation term produces $\overline{c_w^{+\prime} v_w^{+\prime}}$ when the Bachelor sublayer $\delta_B^+ = (\beta_{rms}^+ Sc)^{-1/2}$ is thinner than the viscous sublayer. Under the present flow conditions, $\delta_B^+$ is nearly equal to 0.4 when $Sc_w = 100$. This roughly agrees with the zero-crossing point of the dissipation of $\overline{c_w^{+\prime} v_w^{+\prime}}$ in Fig. 10b. It should be also noted that two major source terms of $\overline{c_w^{+\prime} v_w^{+\prime}}$ at $Sc_w = 100$ in Fig. 10b are the production and dissipation terms, which are tightly linked to the normal velocity fluctuation. This means that the interfacial–normal straining motion associated with the surface divergence is the essential mechanism for generation of $\overline{c_w^{+\prime} v_w^{+\prime}}$.

### 4.5. Mass transfer rate

Eq. (27) can be rewritten in the dimensional form as

$$K_w^* = \frac{Q^*}{\Delta C_{B_w}^*} = A(D_w^* \beta_{rms}^*)^{1/2}. \tag{31}$$

The dimensionless proportional constant of $A$ has fallen within 0.2–0.7 in the previous studies. McCready et al. [24] carried out numerical simulation of a simplified two-dimensional transport equation and concluded that $A = 0.71$. The LES data of Calmet and Magnaudet [16] and Magnaudet and Calmet [17] suggested $A = 0.6$ for both shear-free and sheared interfaces. Note that their definition of $\Delta C_{B_w}^*$ in Eq. (31) is the concentration difference

between the interface and $y = L$, where $L$ is an integral eddy scale. If we use the same definition, $A$ in the present study is slightly increased by 4%. The grid-stirred tank data of McKenna and McGillis [13] lead to $A \sim 0.5$ for a clean interface and $A \sim 0.3$ for a contaminated interface. The wind-wave channel data of Turney et al. [14] suggested $A = 0.45$. Banerjee et al. [15] reported that a value of $A = 0.45$ predicts their DNS data. The experimental data of Tamburrino and Gulliver [12] and Law and Khoo [11] for shear-free and sheared interfaces suggested $A = 0.24$ and 0.22, respectively.

It is quite interesting that most of the previous data for a clean interface concentrated around $A = 0.4$–$0.5$. This value agrees with the present hybrid DNS/LES data, i.e., $A = 0.40$ and 0.44 for sheared and shear-free interfaces, respectively. Furthermore, these values are close to the value of $A = 0.36$ obtained by the one-dimensional transport Eq. (21), although a single sinusoidal wave is assumed for the velocity fluctuation. These results suggest that the balance between the advection and diffusion terms determines the local mass flux under a variety of flow conditions.

Finally, we briefly remark the relationship between the surface divergence model and the conventional surface-renewal model. Eq. (3) is identical to Eq. (31) if we take the response time-scale $1/\beta^*_{\mathrm{rms}}$ as the surface-renewal time $\tau^*_s$. However, the original surface-renewal concept proposed by Danckwerts [3] divides the transport process into advection and diffusion processes, and assumes that the two separate processes alternatively occur at every time period of surface-renewal $\tau^*_s$. This is in contrast to the surface divergence model, where the balance of the advection and diffusion terms determines the local mass flux. Since the original surface-renewal model cannot inherently describe convective surface-renewal motion, Fortescue and Pearson [32] improved the model and proposed a two-dimensional eddy-cell model, in which an eddy cell periodically and continuously renews the free surface. Later, this model was further improved by incorporating the ideas of the time/space fraction of the surface-renewal events [8,23]. In the improved eddy-cell models, the surface-renewal time is represented by the ratio of the typical velocity scale to length-scale of the eddy cell. This quantity is essentially the same as the surface divergence. This would be the reason why the mass transfer rate was well estimated by the surface-renewal eddy-cell model for both sheared and shear-free interfaces [7,23].

Recently, the surface divergence model draws attention because it is a quantity that can be directly measured. On the other hand, the surface renewal time $\tau^*_s$, which is critical in the surface-renewal model (3), has to be inferred, since it cannot be directly measured. As pointed out by Turney et al. [14], this might allow remote sensing methods to be used for measuring the surface divergence. This has the potential to provide more reliable estimates of the air–sea gas exchange.

## 5. Conclusions

Numerical simulation of high Schmidt number mass transfer across a sheared air–water interface was carried out via a hybrid DNS/LES scheme. For a slightly soluble gas considered here, the most concentration change occurs in the water phase. As a result, the air–water interface is almost equivalent to the constant concentration boundary for the water phase. In contrast, the concentration fluctuation in the air phase has a peak at the interface due to the impingement of fresh water on the interface.

Because of the large density ratio, the dynamical coupling between the air and water turbulent flows was found to be quite weak at the low wind velocity considered here. Instead, the self-sustaining mechanisms due to the mean shear govern turbulence in the water phase. The spatio-temporal correlations and the visualizations of the velocity and concentration fields reveal that the surface divergence induced by the quasi-streamwise vortices in the water phase controls the interfacial mass transfer.

In order to investigate quantitative relationship between the local mass flux and the surface divergence, a one-dimensional advection–diffusion equation was analyzed. In this model, the fluctuating surface divergence is modeled as $\beta^+(t^+) = \sqrt{2}\beta^+_0 \cos(\omega^+_0 t^+)$. It is shown that the concentration field near the interface is governed by the ratio of the response time-scale $1/\beta^+_0$ and the renewal time-scale $1/\omega^+_0$. The fluctuating surface divergence contributes to the mass transfer only when $\beta^+_0/\omega^+_0 > 1$, and if this is the case, the local mass transfer rate can be estimated from the surface divergence by the Chan and Scriven's stagnation flow model (25). This would be a primary reason why the mass transfer rate has been successfully correlated with the intensity of the surface divergence under a wide range of flow conditions.

The present analysis showed that the surface divergence model is valid only when $\beta^+_0/\omega^+_0 > 1$. In a highly contaminated interface, however, the surface divergence is strongly damped and does not satisfy this condition anymore. Consequently, the mass transfer rate falls down to the value at a solid surface [9]. Also, for the decaying free-surface turbulence considered in Pan and Banerjee [33], counter-rotating vortices persist at the interface and die out very slowly. In this situation, the tangential components of the convection terms in the original transport Eq. (16) should also be important. Development of the mass transfer model in such flow fields remains to be future work.

## Acknowledgments

The present work was partially supported through the 21st Century COE Program, "Mechanical Systems Innovation," and Grant-in-Aid for Young Scientists (B), 19760131, 2007 by the Ministry of Education, Culture, Sports, Science and Technology in Japan.

## References

[1] B. Jähne, H. HauBecker, Air–water gas exchange, Annu. Rev. Fluid Mech. 30 (1998) 443–468.
[2] M.A. Donelan, R. Wanninkhof, Gas transfer at water surfaces – concepts and issues, in: M.A. Donelan, W.M. Drennan, E.S. Saltzman, R. Wanninkhof (Eds.), Gas Transfer at Water Surfaces, The American Geophysical Union, Washington, 2002, pp. 1–10.
[3] P.V. Dankwerts, Significance of liquid-film coefficients in gas absorption, Ind. Eng. Chem. 43 (6) (1951) 1460–1467.
[4] G.E. Fortescue, J.R.A. Pearson, On gas absorption into a turbulent liquid, Chem. Eng. Sci. 22 (9) (1967) 1163–1176.
[5] S. Banerjee, E. Rhodes, D.S. Scott, Mass transfer to falling wavy liquid films in turbulent flow, Ind. Eng. Chem. Fund. 7 (1) (1968) 22–27.
[6] J.C. Lamont, D.S. Scott, An eddy cell model of mass transfer into the surface of a turbulent liquid, AIChE J. 16 (1970) 513–519.
[7] S. Komori, Y. Murakami, H. Ueda, The relationship between surface-renewal and bursting motions in an open-channel flow, J. Fluid Mech. 203 (1989) 103–123.
[8] M. Rashidi, G. Hetsroni, S. Banerjee, Mechanism of heat and mass transport at gas–liquid interfaces, Int. J. Heat Mass Transf. 34 (7) (1991) 1799–1810.
[9] Y. Hasegawa, N. Kasagi, Systematic analysis of high Schmidt number turbulent mass transfer across clean, contaminated and solid interfaces, Int. J. Heat Fluid Flow 29 (3) (2008) 765–773.
[10] W.C. Chan, L.E. Scriven, Absorption into irrotational stagnation flow – a case study in convective diffusion theory, Ind. Eng. Chem. Fund. 9 (1) (1970) 114–120.
[11] C.N.S. Law, B.C. Khoo, Transport across a turbulent air–water interface, AIChE J. 48 (9) (2002) 1856–1868.
[12] A. Tamburrino, J.S. Gulliver, Free-surface turbulence and mass transfer in a channel flow, AIChE J. 48 (12) (2002) 2732–2743.
[13] S.P. McKenna, W.R. McGillis, The role of free-surface turbulence and surfactants in air–water gas transfer, Int. J. Heat Mass Transf. 47 (3) (2004) 539–553.

[14] D.E. Turnery, W.C. Smith, S. Banerjee, A measure of near-surface fluid motions that predicts air–water gas transfer in a wide range of conditions, Geophys. Res. Lett. 32 (4) (2005) L04607.
[15] S. Banerjee, D. Lakehal, M. Fulgosi, Surface divergence models for scalar exchange between turbulent streams, Int. J. Multiphase Flow 30 (7–8) (2004) 963–977.
[16] I. Calmet, J. Magnaudet, High-Schmidt number mass transfer through turbulent gas–liquid interfaces, Int. J. Heat Fluid Flow 19 (5) (1998) 522–532.
[17] J. Magnaudet, I. Calmet, Turbulent mass transfer through a flat shear-free surface, J. Fluid Mech. 553 (2006) 155–185.
[18] Y. Hasegawa, N. Kasagi, Effects of interfacial velocity boundary condition on turbulent mass transfer at high Schmidt numbers, Int. J. Heat Fluid Flow 28 (6) (2007) 1192–1203.
[19] M. Germano, U. Piomelli, P. Moin, W. Cabot, A dynamic subgrid-scale eddy viscosity model, Phys. Fluids A3 (7) (1991) 1760–1765.
[20] P. Lombardi, V. De Angelis, S. Banerjee, Direct numerical simulation of near-interface turbulence in coupled gas–liquid flow, Phys. Fluids 8 (6) (1996) 1643–1665.
[21] T.J. Hanratty, Effect of gas flow on physical absorption, in: S.C. Wilhelms, J. Gulliver (Eds.), Air–Water Gas Transfer, American Society of Civil Engineers Publisher, New York, 1991, pp. 10–33.
[22] B. Jähne, K.O. Münnich, R. Bösinger, A. Dutzi, W. Huber, P. Libner, On the parameters influencing air–water gas exchange, J. Geophys. Res. 92 (C2) (1987) 1937–1949.
[23] S. Komori, R. Nagaosa, Y. Murakami, Turbulence structure and mass transfer across a sheared air–water interface in wind-driven turbulence, J. Fluid Mech. 249 (1993) 161–183.
[24] M.J. McCready, E. Vassiliadou, T.J. Hanratty, Computer simulation of turbulent mass transfer at a mobile interface, AIChE J. 32 (7) (1986) 1108–1115.
[25] B.H. Brumley, G.H. Jirka, Air–water transfer of slightly soluble gases: turbulence, interfacial processes and conceptual models, Physicochem. Hydrodyn. 10 (3) (1988) 295–319.
[26] G.K. Bachelor, Small-scale variation of convected quantities like temperature in turbulent fluid. Part 1: General discussion and the case of small conductivity, J. Fluid Mech. 5 (1) (1959) 113–133.
[27] W.K. Lewis, W.G. Whitman, Principles of gas absorption, Ind. Eng. Chem. 16 (1924) 1215–1220.
[28] B. Perot, P. Moin, Shear-free turbulent boundary-layers. 1: Physical insights into near-wall turbulence, J. Fluid Mech. 295 (1995) 199–227.
[29] J. Magnaudet, High-Reynolds-number turbulence in a shear-free boundary layer: revisiting the Hunt–Graham theory, J. Fluid Mech. 484 (2003) 167–196.
[30] H. Kawamura, K. Ohsake, H. Abe, K. Yamamoto, DNS of turbulent heat transfer in channel flow with low to medium-high Prandtl number, Int. J. Heat Fluid Flow 19 (5) (1998) 482–491.
[31] D. Lakehal, M. Fulgosi, G. Yadigaroglu, S. Banerjee, Direct numerical simulation of turbulent heat transfer across a mobile, sheared gas–liquid interface, ASME J. Heat Transf. 125 (6) (2003) 1129–1139.
[32] G.E. Fortescue, J.R.A. Pearson, On gas absorption into a turbulent liquid, Chem. Eng. Sci. 22 (9) (1967) 1163–1176.
[33] Y. Pan, S. Banerjee, A numerical study of free-surface turbulence in channel flow, Phys. Fluids 7 (7) (1995) 1649–1664.